Journal of Sound and Vibration (2001) **244**(2), 235–257
doi:10.1006/jsvi.2000.3469, available online at http://www.idealibrary.com on IDEAL®

ON THE WAVEGUIDE MODELLING OF DYNAMIC STIFFNESS OF CYLINDRICAL VIBRATION ISOLATORS. PART II: THE DISPERSION RELATION SOLUTION, CONVERGENCE ANALYSIS AND COMPARISON WITH SIMPLE MODELS

L. KARI

MWL, Department of Vehicle Engineering, Kungliga Tekniska Högskolan, 100 44 *Stockholm, Sweden.*
E-mail: leifk@fkt.kth.se

(*Received* 10 *May* 1999, *and in final form* 5 *October* 2000)

Based on a waveguide model presented in a companion paper (L. Kari 2001 *Journal of Sound and Vibration* **244**, 211–233 [1]), the influences of higher order modes and structure-borne sound dispersion on the axial dynamic stiffness for cylindrical vibration isolators are investigated. On the whole, a moderate mode number results in an accurate stiffness prediction while an accurate stress point value prediction requires more modes. The dispersion relation is solved by a modified Newton–Raphson method with initial values given by an asymptotic expansion or a winding integral method. The integral technique is based on the argument principle; but, as the square root operators in the dispersion relation yield branch points, some modifications are needed. To create single-valued functions conforming to the argument principle, the winding integral search domain is split into branch cut absent subdomains, containing adaptively defined square root operators. The subregion method used for the fulfilment of the boundary conditions at the lateral surfaces is shown to converge faster than for the point-matching method. However, the latter reveals a similar convergence rate as the former at overdetermination. Comparisons with simple stiffness models are made. These models, known as the long rod, the Love, the Bishop, the Kynch, the Mindlin and Herrmann and the Mindlin and McNiven theories are shown to diverge substantially from the presented "exact" theory. To a great extent, the pertinent stress and displacement fields, derived from the presented waveguide model, explain the discrepancies reported for the approximate theories.

1. INTRODUCTION

The great variety of commercially available isolators enables the most diverse vibration isolation problems to be solved, though in many cases custom-designed resilient elements are applied. In a companion paper [1] a waveguide technique was presented, resulting in the axial dynamic stiffness for one of the most common resilient elements: namely, the circular cylindrical vibration isolator in Figure 1 with bonded end plates. The model and the measurements are shown to agree strikingly well within the whole frequency range.

A closed-form dynamic stiffness solution is difficult, arising from the stress singularities at the rubber cylinder corners, the complex constitutive relation and the imposed boundary conditions. In particular, the boundary conditions on the bonded rubber cylinder ends are locally non-mixed; that is, only the displacement components (present case) or the stress

0022-460X/01/270235 + 23 $35.00/0

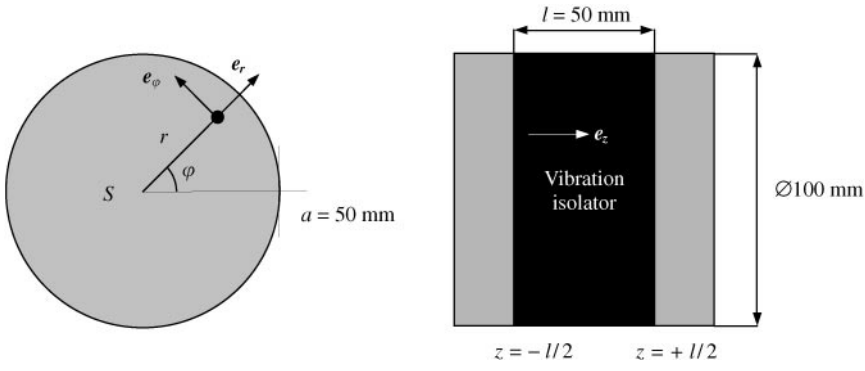

Figure 1. Cylindrical vibration isolator.

components are specified. This obstructs the modelling, grouping it into a non-separable category [2].

The most straightforward method is probably by the mode-matching technique as successfully applied in electric and magnetic waveguide problems [3]. To this end, the axial dependence is separated, the eigenvalues and eigenmodes of the cross-section are calculated, where (provided these modes constitute a complete set) the total field is obtained by eigenmode superposition, finally matching them to the cylinder end boundary conditions.

In the last century Pochhammer [4] and Chree [5] had already developed the dispersion relations for an infinite, elastic rod; that is, the axially independent problem, but without material damping. It took, however, more than 80 years for Onoe *et al.* [6] to resolve its complete axial eigenvalue spectrum, mainly by establishing cut-off frequencies, asymptotic behaviour and a boundary line grid. This method is not suitable for viscoelastic materials, such as rubber. In this paper the spectrum is calculated by a modified Newton–Raphson method [7], with initial values given by an asymptotic expansion or a winding integral method [8]. The integral technique is based on the argument principle; but, as the square root operators in the dispersion relation yield branch points, some modifications are needed. To create single-valued functions conforming to the argument principle, the winding integral search domain is split into branch cut absent subdomains, containing adaptively defined square root operators. The somewhat complicated axial wavenumber spectrum applies a nearly incompressible material model, with the material parameters optimized with respect to the calculated and measured isolator transfer stiffness. The displacement boundary conditions at the rubber cylinder ends are satisfied by a circle-wise fulfilment or a subregion method. In order to fully accept the method, the convergence of the solution must be examined.

Love [9] points out that the real eigenvalues to the dispersion relation (without material damping) are finite in number at a given frequency. This is also the case for the imaginary eigenvalues. Thus, the corresponding eigenmodes cannot themselves form a complete set, in which to expand an arbitrary cylinder end boundary condition. However, Adem [10] shows that there are also an infinite number of complex eigenvalues, rendering a complete set possible. The prevalence of approximate cylinder waveguide theories among engineers seems to grow from a lack of awareness of these complex eigenvalues, the dispersion relation complexity and from the difficulties of simultaneously satisfying the boundary conditions at the lateral and radial surfaces. These approximations are deliberately used known as the long rod [11], the Love [9], the Bishop [12], the Kynch [13], the Mindlin and

Herrmann [14] and the Mindlin and McNiven [15] theories, no matter how ineptly, in various applications.

In this paper the dispersion relation solution, convergence analysis and comparison with simple models are the study focus, thus rendering the presentation in Part I [1] more comprehensive.

2. EIGENMODES AND EIGENVALUES

The axially symmetric and non-torsional part of the dispersion relation for an infinite cylinder with radius a (equation (20) in reference [1] or equation (8.2.41) in reference [16]), is reformulated as (1)

$$\begin{aligned} a[k_T^2 - 2k_z^2]^2 \, \mathrm{J}_0(\sqrt{k_L^2 - k_z^2}\, a) \, \mathrm{J}_1(\sqrt{k_T^2 - k_z^2}\, a) \\ + 4ak_z^2 \sqrt{k_L^2 - k_z^2} \sqrt{k_T^2 - k_z^2} \, \mathrm{J}_0(\sqrt{k_T^2 - k_z^2}\, a) \, \mathrm{J}_1(\sqrt{k_L^2 - k_z^2}\, a) \\ = 2\sqrt{k_L^2 - k_z^2}\, k_T^2 \, \mathrm{J}_1(\sqrt{k_L^2 - k_z^2}\, a) \, \mathrm{J}_1(\sqrt{k_T^2 - k_z^2}\, a), \end{aligned} \tag{1}$$

to yield $k_{z,n}$ as a target parameter in search of eigenvalues ($k_z \neq k_T$), where the order $n \in \mathbb{Z}_+$, J_m is the Bessel function of the first kind and order m and k_z, k_L and k_T are axial, longitudinal and shear wave numbers. The search is restricted to $\Re k_z \geqslant 0$ and $\omega \geqslant 0$. The extension to the left-hand half of the k_z-plane is performed by the formal replacement of $k_{z,n} \leftarrow -k_{z,n}$, as the dispersion relation (1) is an even function of the axial wave number. To find the roots at a specific frequency, initial values are computed, then an iterative method determines the roots to the desired accuracy.

The initial values are found by a winding integral method or by an asymptotic expansion of the dispersion relation. Expansion is applied only for large $|k_z|$ while the integral method is used for small and moderate magnitudes with domains partly overlapped to provide a reliable transition between the methods. Although the integral method can be used for the whole search region, the technique is tedious and time-consuming, whereas expansion is more cost effective, but feasible only for large $|k_z|$.

After a lengthy but straightforward asymptotic expansion of the transcendental equation (1), the eigenvalues are approximately

$$k_z \approx \frac{1}{2a}[\pm \log_e(4p\pi) \pm 2p\pi \mathrm{i}], \tag{2}$$

[17] where $1 \ll p \in \mathbb{Z}_+$. It is observed that the asymptotic eigenvalues are independent of frequency and material properties, making it necessary to calculate the set of asymptotic initial values only once, thus avoiding numerical computations.

The winding integral method is based on the argument principle. That is, the total argument variation of a meromorphic function around, in the counter clockwise sense, a closed single path equals 2π times the difference between the number of zeros and poles, counted with multiplicity, within the complex region enclosed by the path. Without modifications, the path is not allowed to pass through any zero or singularity of the function. The dispersion relation (1) is, however, not ideally suited for the argument principle, due to the branch points for the square root operator at $k_z = \pm k_L$ and $k_z = \pm k_T$. In order to create a single-valued function, the single domain may be replaced by a two-sheeted Riemann surface at each branch point. In principle, it is possible to enforce

the search region to remain within the first Riemann sheet, but the discontinuous phase changes across the branch cuts are, in general, too large to be convenient.

The directions of the branch cuts, radiating from the branch points, are mathematically arbitrary. The problem is therefore encompassed by excluding a small domain at each branch point and splitting the remaining search domain into several subdomains. The square root operator is adaptively defined for each subdomain to avoid any branch cut within the subdomain. In particular, the branch cut in the $(k_{(\cdot)}^2 - k_z^2)$-domain may be adapted along the negative or along the positive real axis. For $\Re k_z \geqslant 0$, the image branch cut in the k_z-domain is a "hyperbolic" curve from $k_{(\cdot)}$ to $+\infty$ or to $-\infty\,\mathrm{i}$, respectively. Likewise for $\Re k_z < 0$, the image goes from $-k_{(\cdot)}$ to $-\infty$ or to $+\infty\,\mathrm{i}$, respectively. [Figures 2(a) and (b)]. In particular, a rectangular search domain, enclosing both branch points for $\Re k_z \geqslant 0$, with the sides parallel to the real and imaginary axes is split into 11 subrectangles and two small squares (see Figure 3). Naturally, other splitting configurations and other kinds of search domain, such as circular or triangular shaped, may be used. The adapted branch cuts for the respective subrectangles are given in Table 1. The different branch cuts may, at most, alter the sign of $\pm k_{\perp \mathrm{L}}$ or $\pm k_{\perp \mathrm{T}}$, which has no physical significance. Finally, the argument principle is used to locate, isolate and approximately determine all the roots within each subrectangle [8]. Each eigenvalue is given by its multiplicity and the lower left and upper right corners of an optional small rectangle enclosing the root. Although any value within the small rectangle, such as the centre point, is applicable as an initial value, the point given by the first moment of winding number integral, $k_{z0} = (1/2\pi\mathrm{i}) \oint_{\partial R} k_z \,\mathrm{d}[\log F(k_z)]$, is preferred, where ∂R is the boundary of the small rectangle and F is the dispersion relation in a non-dimensional form.

Once the initial values are computed by the asymptotic expansion or the winding integral method, an iterative method is used to determine the eigenvalues to their desired accuracy. The Newton–Raphson method is suitable as the partial derivative, with respect to k_z, of the dispersion relation can be readily determined. The algorithm is adaptively damped, for initial values given by the winding integral method, in order to enforce the iterations to remain within the small initial rectangles. In addition, the quadratic convergence of the Newton–Raphson method is maintained at multiple roots by a modified iteration algorithm, [7].

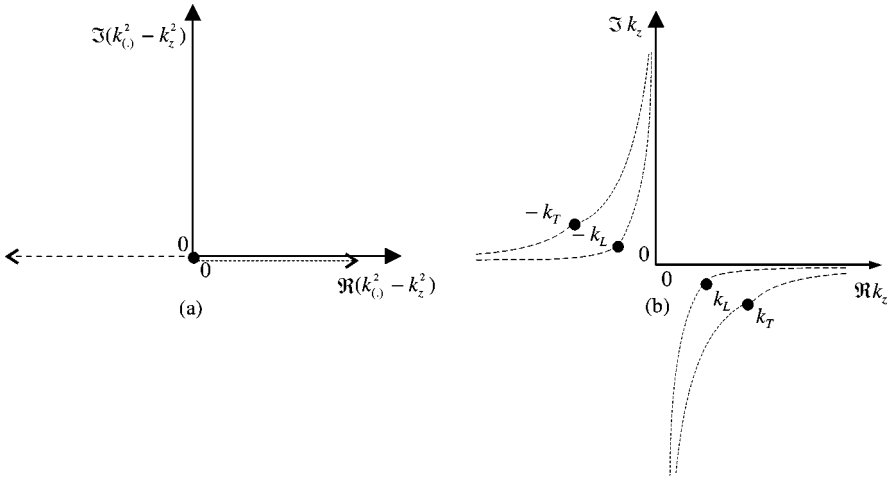

Figure 2. (a) Adapted branch cuts along negtive (dashed) and positive real axis (dotted) for $\sqrt{k_{(\cdot)}^2 - k_z^2}$ and (b) resulting branch cuts in k_z-plane.

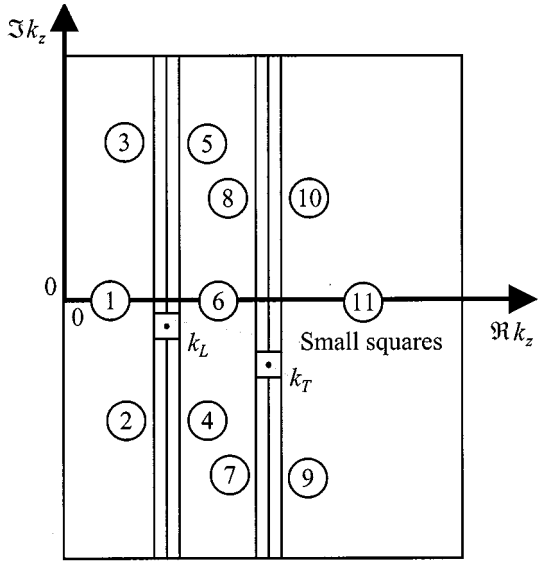

Figure 3. Search rectangle split.

TABLE 1

Adapted negative or positive real axis as branch cut in $(k_{(\cdot)}^2 - k_z^2)$*-domain*

Negative or positive real axis as branch cut in $(k_{(\cdot)}^2 - k_z^2)$-domain		
Subrectangle	$\sqrt{k_L^2 - k_z^2}$	$\sqrt{k_T^2 - k_z^2}$
1–3	Negative	Negative
4–8	Positive	Negative
9–11	Positive	Positive

A "quicksort" routine arranges the axial eigenvalues in an increased spatial attenuation order, as $|\mathscr{T} k_{z,n}| \leqslant |\mathscr{T} k_{z,m}|$; $n < m$; $n, m \in \mathbb{Z}_+$.

A rapid determination of the eigenvalues, for a range of frequencies, is to perform the operations above for the first frequency, then use the calculated roots as initial values to the Newton–Raphson method for the second frequency. The eigenvalues for the remaining frequencies are determined by the Newton–Raphson method using the extrapolated eigenvalues from the two preceding frequencies as initial values. A more reliable procedure is to perform the same operations for all frequencies as for the first frequency above. Although this is time-consuming, the operations discount the size of the frequency step.

Next, the procedure above is applied to the actual vibration isolator. The first 100 eigenvalues at 50, 250, 500, 1000, 3000, 5000, 8600 and 10000 Hz are shown in Figure 4. The real axes are auto scaled while imaginary axes are fixed in the whole frequency range. The eigenvalues are plotted as points, with those corresponding to propagating modes surrounded by circles. Propagating modes do not formally exist for viscoelastic materials but for elastic materials. Whether a mode is propagating or not is, therefore, deduced from

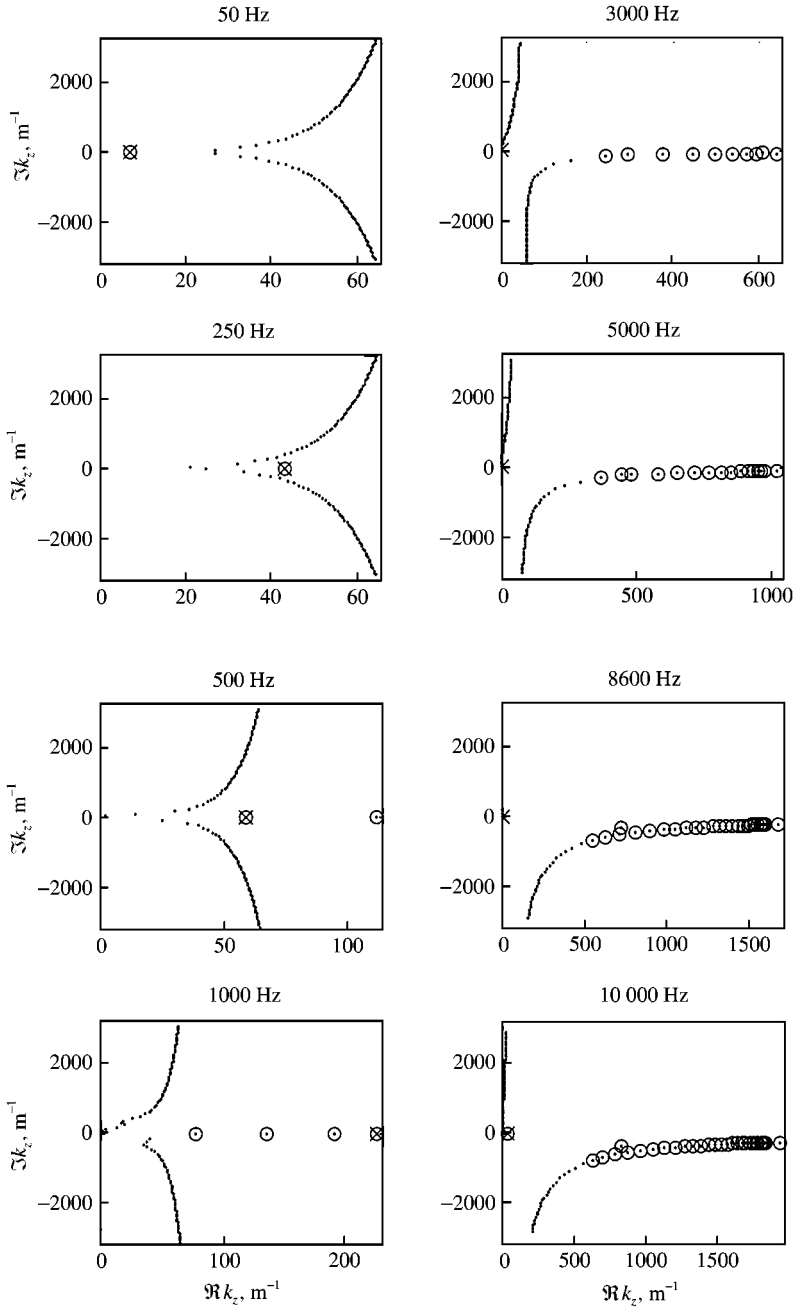

Figure 4. The first 100 axial eigenvalues. Propagating mode (0) and min $|\Im k_z|$(×); 50–10 000 Hz.

the cut-on frequency for its elastic counterpart, derived by means of the formal replacement $\tilde{\mu} \leftarrow \Re\tilde{\mu}$.

The number of propagating modes grows rapidly, being 1 + 0 at 50 Hz, 1 + 0 at 250 Hz, 2 + 0 at 500 Hz, 4 + 0 at 1000 Hz, 10 + 0 at 3000 Hz, 16 + 0 at 5000 Hz, 27 + 0 at 8600 Hz and 31 + 1 at 10 000 Hz, where x and y in $x + y$ refer to "axial" and "radial" modes

respectively. The terms originate from the displacement pattern identified with the corresponding elastic mode, being essentially axial and radial respectively as $|k_z| \to 0^+$. For non-vanishing axial eigenvalues the displacement of a given mode generally involves contributions from both components. In principle, the larger the eigenvalue, the higher the contributions from the other component. Besides, every axial eigenvalue for viscoelastic materials are non-zero when $f \neq 0$. In this connection and for later economy the terms merely facilitate the classification of the eigenvalue spectra rather than reflect their precise literal sense.

The eigenvalues corresponding to the non-propagating modes approach the asymptotic eigenvalues, given by equation (2), when $1 \ll p \in \mathbb{Z}_+$, whereas the eigenvalues are somewhat jumbled for smaller p, as shown in Figure 4. As the frequency increases and $\Re k_z \geqslant 0$, the intermediary eigenvalues advance against the imaginary axis for $\Im k_z > 0$, or distance themselves from the same for $\Im k_z < 0$. Accordingly, the minimum p for close prediction by equation (2) increases with increasing frequency, being more than 50 for $f \geqslant 3000$ Hz. Consequently, the asymptotic, frequency-independent eigenvalues are of little value for $f \geqslant 3000$ Hz and $M < 100$, as $M \approx 2p$ when $1 \ll p \in \mathbb{Z}_+$.

The non-propagating modes on the lateral surfaces of the cylinder as discussed in section 4 are important. These mode eigenvalues are, for elastic materials, split into complex and purely imaginary eigenvalues, both modes represent near-fields, but those for complex eigenvalues also involve spatially oscillating factors. The eigenvalues for elastic materials have the additional symmetry $k_z^* \leftrightarrow k_z$. Consequently, complex eigenvalues occur in fours, one in each of the four quadrants, whereas the real and imaginary ones occur in pairs. As energy dissipation in elastic material is impossible, a complex eigenvalue mode must be augmented with its dual from another quadrant. Consider, for example, a semi-infinite cylinder extended in the positive z direction with the lateral surface at $z = z_0$, $z_0 \in \mathbb{R}$. The sums of the complex eigenvalue modes in the third and the fourth quadrants represent semi-infinite standing waves with vanishing amplitudes as $z \to \infty$. Likewise, the corresponding mode sums for the first and the second quadrants represent semi infinite standing waves for a semi-infinite cylinder extended in the negative z direction.

Regarding modes with real eigenvalues in infinite or semi-infinite cylinders of elastic materials, the group velocity of these modes may have the opposite sign to the corresponding phase velocity, that is, $(\omega/k_z)\,\partial\omega/\partial k_z < 0$, occasionally. The sound choice of the real eigenvalues are those with correct sign of the group velocity. All the eigenvalues must, however, be used for finite cylinders. Taking into consideration that all the eigenvalues for the modes in viscoelastic cylinders are complex for $f \neq 0$, similar arguments as above are applicable to those cylinders.

In order to distinguish the mode with the lowest attenuation per unit axial length, the eigenvalue obeying $\min|\Im k_z|$ is x-marked in the plots of Figure 4. It is particularly noteworthy that this eigenvalue mode does not belong to the propagating modes on the plots at 3000–8600 Hz. Nevertheless, this low attenuation radial mode strongly influences the field from $\sim$ 2000 to 10000 Hz. For frequencies above $\sim$ 8600 Hz it is propagating with the eigenvalue close to the real axis, while below this frequency the mode is non-propagating close to the imaginary axis. The mode's importance is due to its low attenuation, but as the real part of the mode's eigenvalue is also small, its axial wavelength is correspondingly large. The importance of the lowest attenuation mode is also established by examining its mode coefficient, being several orders larger than for the propagating modes. Around and above the cut-on frequency, the stiffness goes through an anti-resonance. The eigenvalue with its opposite sign dual is shown in Figure 5, in the range of 8500–8700 Hz. Figure 5(a) shows a three-dimensional graph with the real and imaginary parts of $k_{z,1}$ on the horizontal axis and the frequency on the vertical axis. Figures 5(b) and (c)

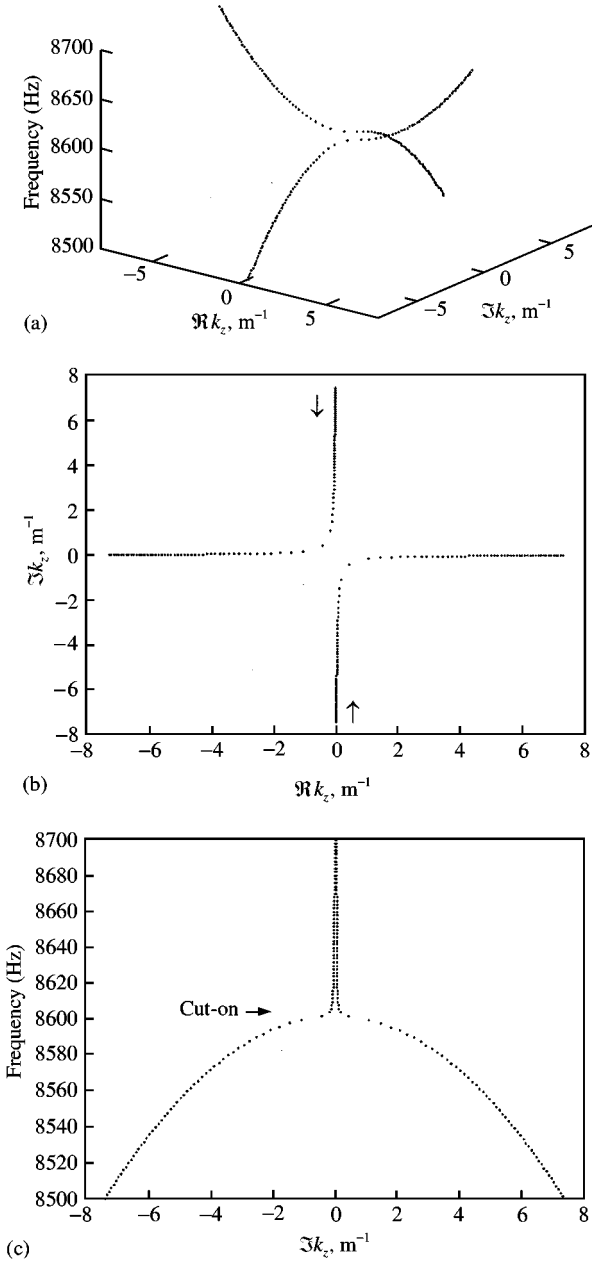

Figure 5. (a) Eigenvalue to lowest attenuation mode and its dual; 8500–8700 Hz, step 2 Hz. (b) The 3-D graph in (a) viewed from positive frequency axis. Direction of increasing frequency marked. (c) The 3-D graph in (a) viewed from positive real axis. Cut-on frequency marked.

show the same viewed from the positive frequency axis and from the positive real axis respectively. As the frequency increases in Figure 5(b), the eigenvalue in the first quadrant is transferred to the second quadrant and the one in the third quadrant to the fourth quadrant. The cut-on frequency is distinct in Figure 5(c).

Finally, a survey of the eigenvalues, showing only those inside the box $0 \leqslant \Re k_z \leqslant 2000$ and $-1000 \leqslant \Im k_z \leqslant 1000\,\mathrm{m}^{-1}$, is in Figures 6(a)–(d), in the whole range of 50–10 000 Hz.

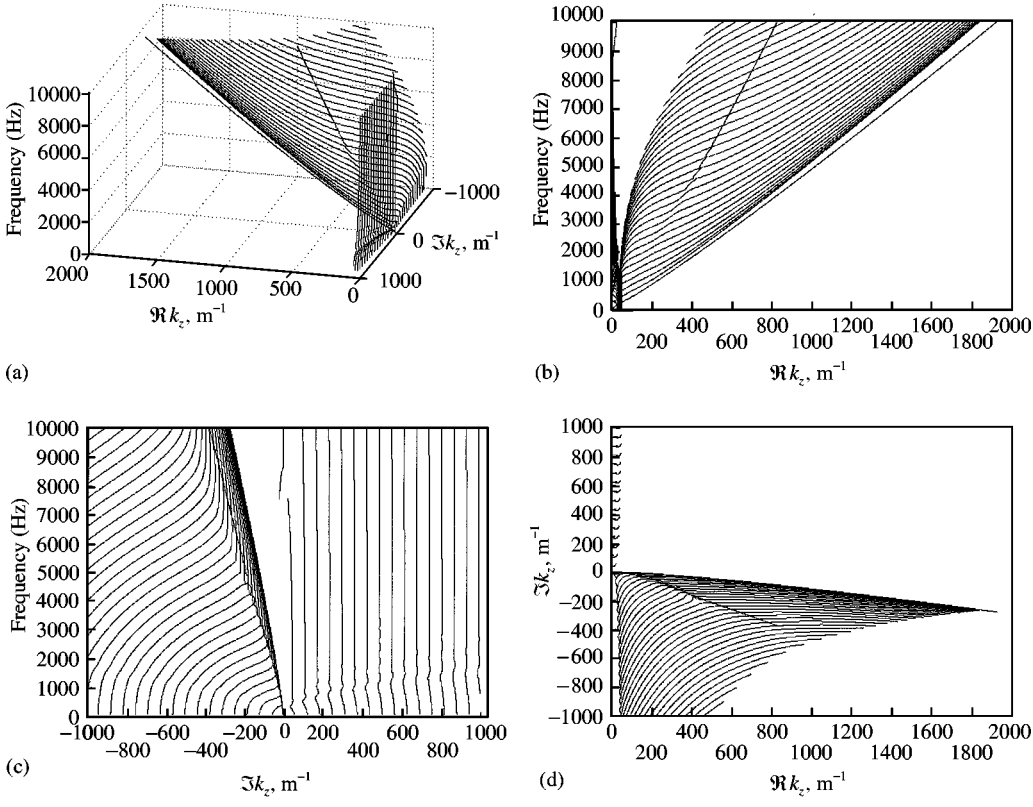

Figure 6. (a) A survey of eigenvalues. (b) The 3-D graph in (a) viewed from negative imaginary axis (c) The 3-D graph in (a) viewed from positive real axis. (d) The 3-D graph in (a) viewed from positive frequency axis.

Figure 6(a) shows a three-dimensional graph with the real and the imaginary parts of k_z on the horizontal axes and the frequency on the vertical axis. Figures 6(b)–(d) show the same viewed from the negative imaginary, the positive real and the positive frequency axis respectively. The plots in Figure 4 can be identified as the constant frequency slices of the graph in Figure 6(a).

The rapid growth of propagating modes is readily seen in Figure 6(b), where the eigen-value to the first propagating mode is distinguishable, as continuously propagating, having the Rayleigh phase velocity as its short wavelength limit [16], whereas the neighbouring axial modes have the shear phase velocity as their limit, with one more noticeable eigenvalue particularly divergent from around 5000 Hz.

In Figures 6(c) and (d) the propagating axial modes eigenvalues are shown to deviate gradually from the real axis as the frequency increases. This is quite contradictory to the first propagating radial mode, with its eigenvalue close to the real axis up to 10 000 Hz. This is not surprising, since the radial mode in this frequency range is rather dependent on the bulk modulus, which has a vanishing loss factor in the rubber material model, whereas the loss factor for the shear modulus grows with increasing frequency, causing deviations of the axial modes.

As expected, none of the eigenvalues intersect the vanishing imaginary part plane in Figures 6(c) and (d). A mode with $\Im k_z = 0$ implies no attenuation along the axial direction of the cylinder. This kind of "super conductivity" is, however, physically impossible in viscoelastic materials.

3. COMPARISON WITH SIMPLER MODELS

Owing to the dispersion relation complexity, the lack of awareness of the complex eigenvalues for elastic materials plus the difficulties of simultaneously satisfying the boundary conditions at the lateral and radial surfaces, a number of approximate theories have been developed for finite cylinders. In the context of the present theory, these simpler models contain only a few modes approximating to the current eigenvalue spectra only over a limited range. Nevertheless, the models have been extensively applied over the years with particular emphasis on the simplest.

To test the application of the models on the isolator, six of the most interesting theories are compared to the present theory and measurements. To this end, the material model and parameters for all the stiffness models are the same as in section 3.3, equation (54) in reference [1].

The first is the classical long rod model [11] or [16], which assumes that lateral, plane cross-sections remain plane and lateral, and that uniaxial and uniform stress exists, while radial expansions and contractions arising from axial stress are neglected. The second, the Love model [9], extends the long rod by taking into account the radial displacement, thus exhibiting geometrical dispersion which the long rod does not. However, all six models are inherently dispersive through the material model used, a physical property which can be termed material dispersion. The third, the Bishop model [12], extends the Love theory, including shear stresses due to radial displacements arising from axial stress, predicting two modes, one propagating and one non-propagating. Bishop's two-mode theory includes both, while the single-mode theory neglects the latter. The fourth, the Kynch model [13], extends the Love theory, replacing the Poisson ratio, coupling the axial and radial motions, to a "dynamic" Poisson ratio, which depends on the axial wavelength derived from a variation technique. The fifth, the Mindlin and Herrmann model [14], assumes specific axial and radial displacements. The method includes corrections for strain and kinetic energy associated with radial motion, with results identical to the Volterra method of internal constraints [18]. To enable, for example, the phase velocities to be adjusted for better agreement with those of Pochhammer and Chree, two frequency-dependent parameters are introduced. In particular, the first mode may be adjusted by the first parameter to yield the Rayleigh phase velocity as a short wavelength limit. Here, both parameters are taken as unities (that is, no corrections). The sixth, the Mindlin and McNiven [15], extends the Mindlin and Herrmann theory to an additional mode, expanding the displacements in terms of Jacobi polynomials to obtain suitable equation systems in the radial co-ordinate. These possess convenient orthogonal properties through the cylinder cross-section. The four adjustment parameters of their theory are here taken as unities (that is, no corrections).

First, the models are applied to a very long isolator; 5000 mm long (100 times the original length) and 50 mm radius, where they should coincide. This is also the case in Figure 7 showing transfer and driving point stiffness for all the above models from 1 to 50 Hz.

Next the actual isolator is considered. Figures 8 and 9 show the axial dynamic stiffness. Figures 9(a)–(d) show the driving point stiffness with no plates included, while Figures 8(a)–(d) show the transfer stiffness. The results of the single-mode theories are in Figures 8(a) and (b) and 9(a) and (b), while those of the two- and three-modes theories are in Figures 8(c) and (d) and 9(c) and (d). For comparison, the results of the present theory are shown as thick solid line whilst the measurements are shown as dashed line. The upper frequency is limited to 1000 Hz as the simple models are most suitable in this frequency range.

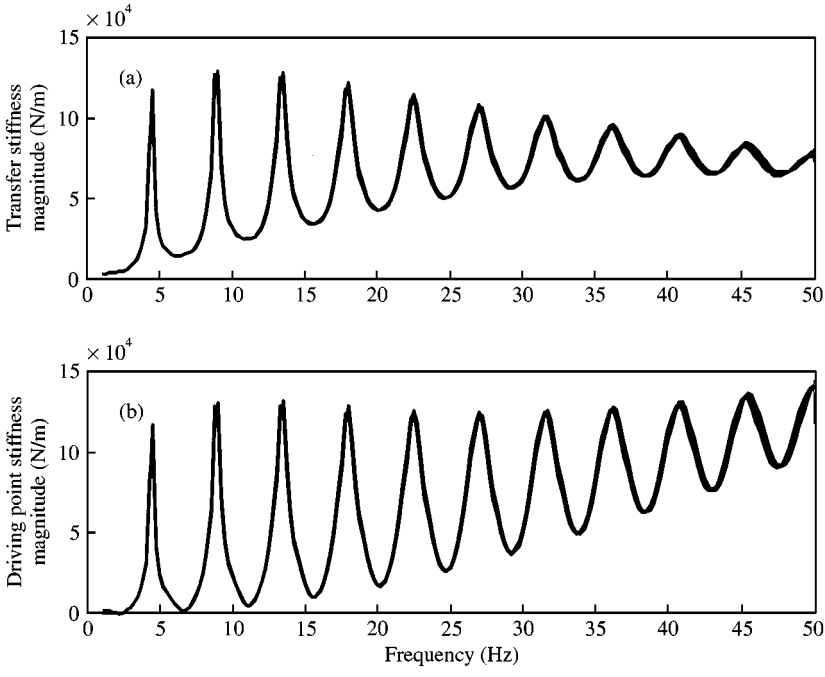

Figure 7. Magnitude of (a) transfer and (b) driving point stiffness for a 5000 mm long isolator ($100 \times l$). Present, long-rod, Love, Bishop 1-mode, Bishop 2-mode, Mindlin and Herrmann, Kynch and Mindlin and McNiven theory (all in solid lines).

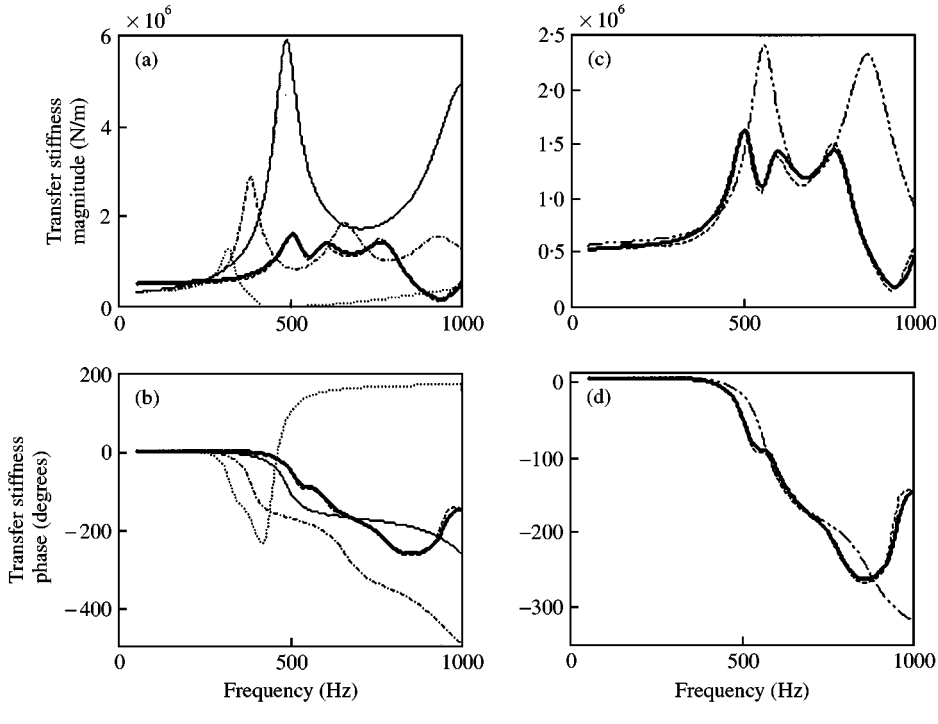

Figure 8. Transfer stiffness. (a) and (b) Present theory (▬▬), measurement (– – – –), long-rod theory (——), Love theory (·····), Bishop 1-mode theory (– · – · –); (c) and (d) Present theory (▬▬), measurement (– – – –), Mindlin and Herrmann theory, Bishop 2-mode theory, Kynch theory and Mindlin and McNiven theory (– · · –).

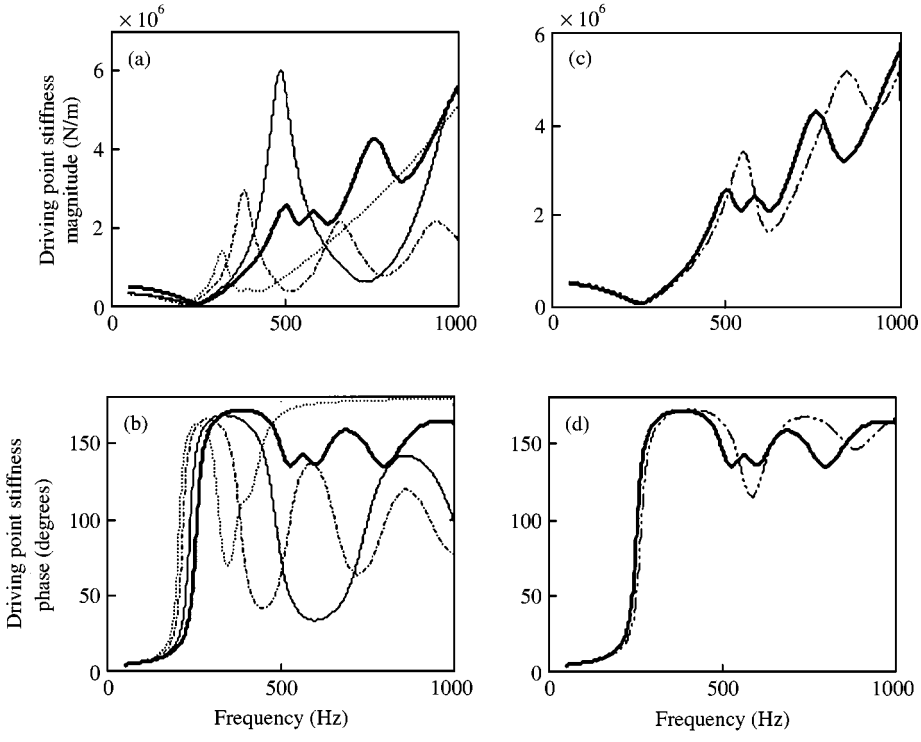

Figure 9. Driving point stiffness. (a) and (b) Present theory (▬▬), long-rod theory (——), Love theory (·····), Bishop 1-mode theory (–·–·–·–); (c) and (d) present theory (▬▬), Mindlin and Herrmann theory, Bishop 2-mode theory, Kynch theory and Mindlin and McNiven theory (–···–).

The approximate methods fail to model the stiffness satisfactorily. In single-mode theories, there is a systematic underestimation of the stiffness at frequencies below 200 Hz, since only the axial displacement boundary conditions are fulfilled. The plates radial constraining effects are, therefore, neglected. The two- and three-modes theories satisfy the boundary conditions but, nevertheless, slightly overestimate the stiffness in the low-frequency range.

The long rod model predicts the first anti-resonance frequency for transfer stiffness and the first resonance and the first anti-resonance frequencies for driving point stiffness fairly well, although those point magnitudes and the remaining curve are poorly predicted. The Love model overestimates the lateral inertia effects, so the mode becomes non-propagating with meagre stiffness predicted above 200 Hz. The single-mode Bishop model overcomes the defect of the overestimation, with results between those of the Love and long rod theories.

The results of the Bishop two-mode, the Kynch, the Mindlin and Herrmann and the Mindlin and McNiven examples coincide within the frequency range considered. These two- and three-mode theories estimate the first resonance frequency for the driving point stiffness very well but the stiffness, in line with the one-mode theories, is incorrectly predicted. By adjusting the first mode of the Mindlin and Herrmann theory to yield the Rayleigh phase velocity as a short wavelength limit (not shown), gives almost the same stiffness results as without adjustments.

The present work is more elaborate than earlier theories, and the results are very close to the measurements whereas the approximate theories fail in this light.

4. CONVERGENCE PROPERTIES OF THE SOLUTION

In order to fully accept the method, the convergence of the solution is examined. To this end, the number of collocation radii and modes is extended; that is (using the notations of section 2 in reference [1]), the P_r^1-, P_z^1-, P_r^2-, P_z^2- and the M-convergence of the solution is verified by their respective extensions. The extension technique, although in other contexts, is frequently applied in finite element methods, as described by Szabó and Babuška [19]. Since this paper aims mainly at dynamic stiffness, the convergence of this global quantity is examined.

The M-extension is processed by calculating the stiffness for $M = 2^n$, $n = 1, 2, \ldots, 7$, by point matching with equidistant collocation radii. Inasmuch as $P_r^1 + P_z^1 + P_r^2 + P_z^2 \geqslant 2M$, the number of collocation radii is concurrently extended according to $P_r^1 = P_z^1 = P_r^2 = P_z^2 = M/2$. The frequency range considered is 50–1000 Hz with the results shown in Figures 10 and 11.

Figures 11(a)–(c) show the driving point stiffness, with no plates included, while Figures 10(a)–(c) show the transfer stiffness. Although the stiffness deviates significantly for small M,

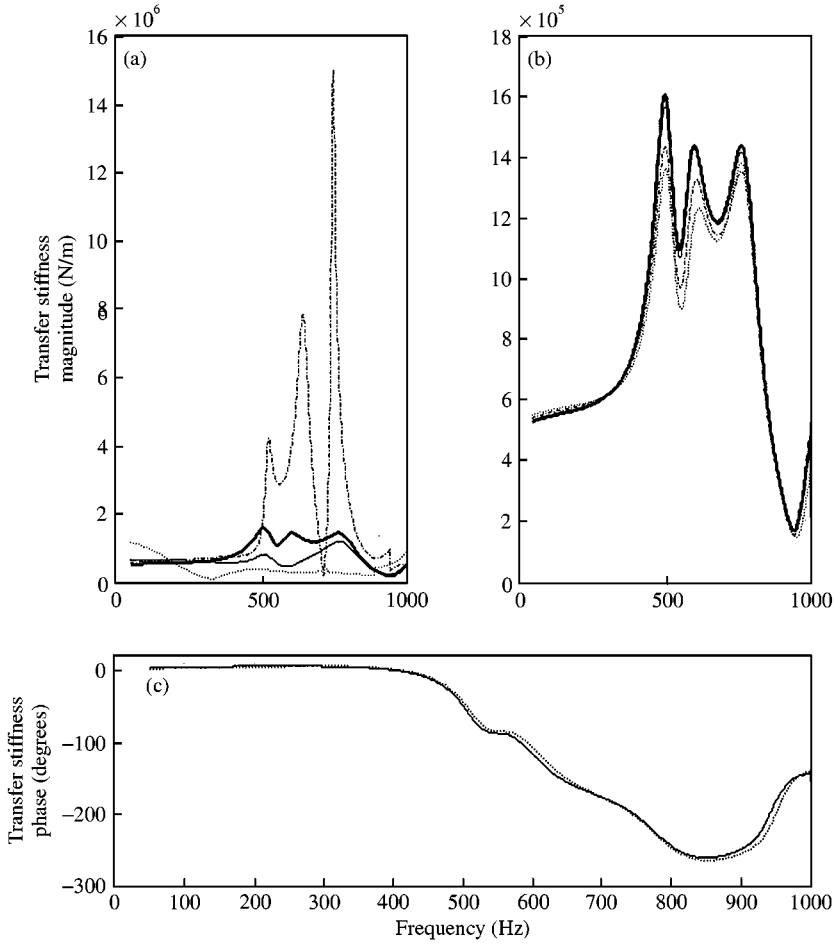

Figure 10. Transfer stiffness. (a) $M = 128$ (▬), $M = 8$ (——), $M = 4$ (–·–·–), $M = 2$ (·····); (b) $M = 128$ (▬), $M = 64$ (——), $M = 32$ (–·–·–), $M = 16$ (·····); (c) $M = 128$, $M = 64$, $M = 32$ (solid), $M = 16$ (·····).

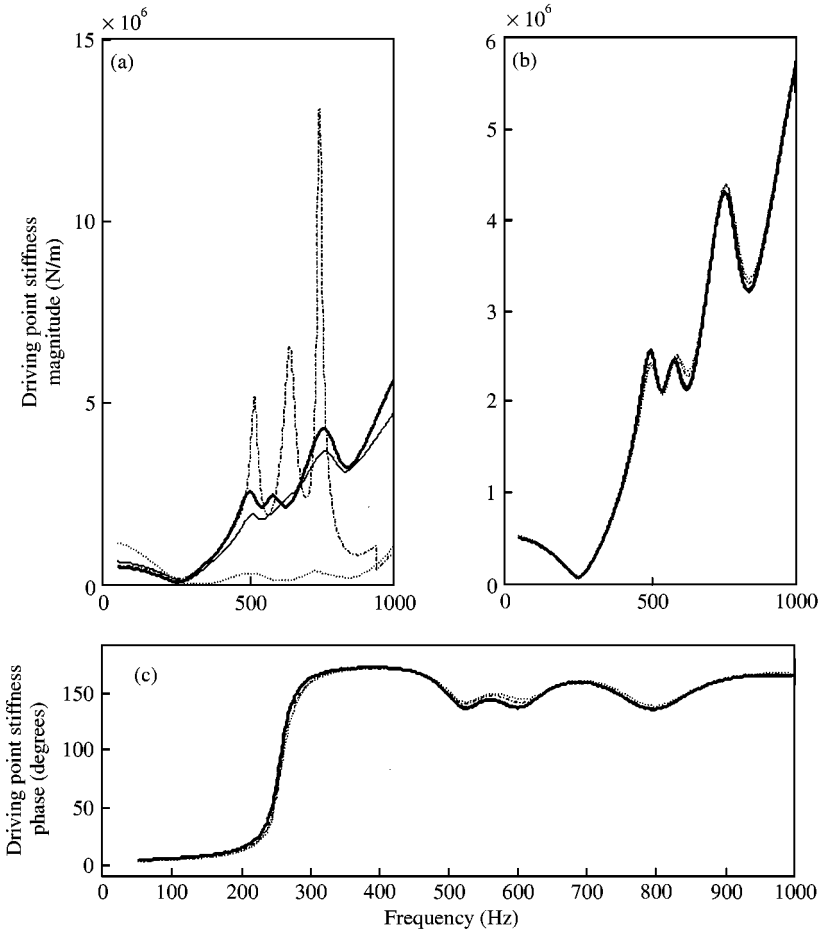

Figure 11. Driving point stiffness. (a) $M = 128$ (▬), $M = 8$ (——), $M = 4$ (–·–·–·), $M = 2$ (·····); (b) and (c) $M = 128$ (▬), $M = 64$ (——), $M = 32$ (–·–·–), $M = 16$ (·····).

it converges for larger M. The difference between $M = 64$ and 128 results is negligible from an engineering point of view.

Although the importance of large M modes declines, they are, nevertheless, important at moderate M. Physically, these moderately high order modes contribute to the fulfilment of the displacement boundary conditions. The fields at these lateral surfaces in turn determine the dynamic stiffness, which is substantially influenced by these higher order modes, as shown clearly in Figures 10 and 11.

In a similar manner, the separate P_r^1-, P_z^1-, P_r^2- and P_z^2-convergences of the solution are established. First, the stiffness is calculated for $P_r^1 + P_z^1 + P_r^2 + P_z^2 = 2M$, and then the $P_{(\cdot)}^{(\cdot)}$-extension is performed. The number of the modes and other radii are constant, with the results analogous to those of the M-extension.

To further study the convergence properties of the solution, the completion level of the displacement boundary conditions equations (15) and (16) in reference [1] is investigated. A simple measure of this completion is the displacement residual variance, normalized with the excitation and is suitable in a practical engineering environment, defined as

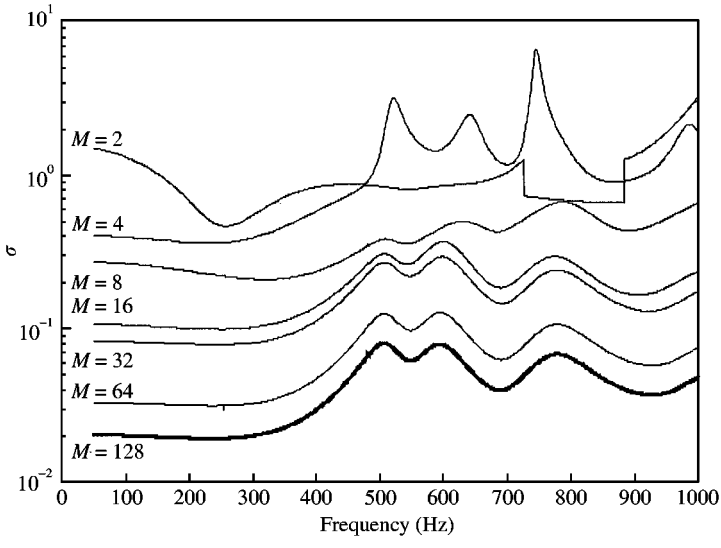

Figure 12. Normalized standard deviation of displacement residual. M indicated at each curve.

$\sigma^2 = [\sigma_1^2 + \sigma_2^2]/2$, where

$$\sigma_1^2 = \frac{1}{\|\tilde{\mathbf{d}}\|_2^2 S} \int_{\partial_d^1 \mathscr{B}} \|\tilde{\mathbf{u}} - \tilde{\mathbf{d}}\|_2^2 \, \mathrm{d}S \tag{3}$$

$$\sigma_2^2 = \frac{1}{\|\mathbf{d}\|_2^2 S} \int_{\partial_d^2 \mathscr{B}} \|\mathbf{u}\|_2^2 \, \mathrm{d}S \tag{4}$$

using the notations of section 2 in reference [1]. The corresponding standard deviations are calculated with the M-extensions above. The results in Figure 12 clearly show the residual decreases as M increases. The sections of the greatest deviations are located nearby the anti-resonances.

In general, derivative operators ruin the convergence. Thus, the dynamic stiffness is believed to converge slowly as the axial stress required for the stiffness derivation is determined by the spatial derivatives of the displacements. Surprisingly, the convergence rate of the stiffness is rather high (as shown in Figures 10 and 11 and discussed above) due mainly to the additional spatial integration of the axial stress (according to equations (18) and (19) in reference [1]). Physically, the integration averages the field and to a great extent cancels out erroneous oscillating terms.

In order to obtain the local quantities, such as displacement and stress, with acceptable accuracy, the errors must be further reduced. A natural choice is to increase the refinement by increasing the number of equidistant collocation radii. In particular, the standard deviation of the displacement discrepancy at 1000 Hz and with $M = 128$ is calculated. The total number of equidistant collocation radii used is 4×64, 4×128, 4×256, 4×512, 4×1024, 4×2048 and 4×4096. That is, the equation system is exactly determined, 1-, 3-, 7-, 15-, 31- and 63-fold overdetermined. The results are in Figure 13. The standard deviation drops instantaneously at single-fold overdetermination but levels off rather promptly. The almost constant deviation for higher order overdeterminations, though small, is mainly due to the truncation of the highest order modes; $M > 128$.

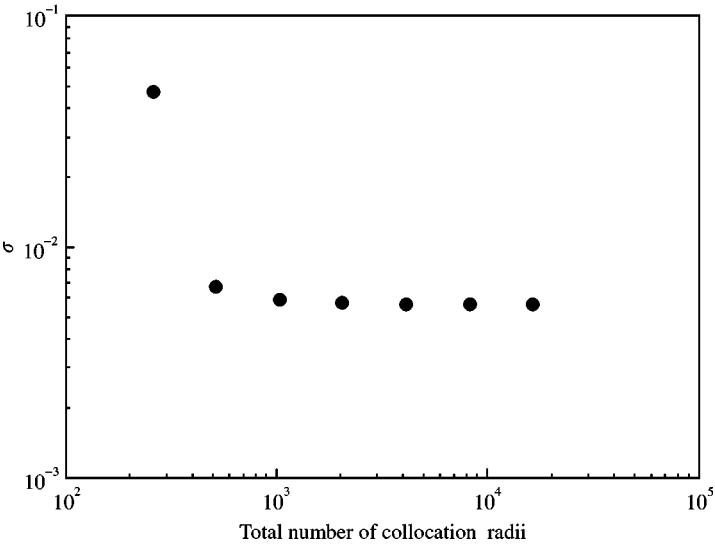

Figure 13. Normalized standard deviation versus total number of collocation radii. $M = 128$, 1000 Hz.

Additional refinement patterns, such as with enhanced refinement close to $r = a$, were tested but the former method seems to be the most suitable.

To investigate the local effects of overdetermination and mode number increase, the stresses and displacements are calculated at $z = l/2$ at 1000 Hz. First, the equation system is exactly determined with $M = 128$. Then it is overdetermined three-fold with $M = 512$. The results are in Figures 14. Figure 14(a) shows the magnitude of the axial displacement while Figure 14(b) the corresponding radial displacement. Likewise, the magnitude of the axial stress is in Figure 14(c) with the radial shear stress in Figure 14(d). All results are normalized with the excitation $|\tilde{\mathbf{d}}|$.

In Figures 14(a) and (b), the displacements with $M = 128$ oscillate strongly, whereas those with $M = 512$ almost vanish, the amplitudes of the oscillations are, however, small, in general being less than 0·015. The rather high standard deviation of $4{\cdot}83 \times 10^{-2}$ with $M = 128$ (shown in Figure 13) is mainly attributed to a poorer fulfilment of the boundary condition at $z = -l/2$. The convergence destroying effects of the spatial derivative operators are clearly shown in Figures 14(c) and (d). The stresses with $M = 128$ oscillate very strongly whereas those with $M = 512$ behave smoothly. At $r = a$ and with $M = 512$ the axial stress is large. This point is singular. Likewise, close to $r = a$ and with $M = 512$, the radial shear stress oscillates slightly but vanishes at $r = a$.

The standard deviation is reduced from $4{\cdot}83 \times 10^{-2}$ with $M = 128$ to $1{\cdot}34 \times 10^{-3}$ with $M = 512$. The magnitude and the phase of the transfer stiffness are altered from $4{\cdot}82 \times 10^{5}$ N/m^2 and -146° to $4{\cdot}86 \times 10^{5}$ N/m^2 and -146°. Likewise, the driving point stiffness is altered from $5{\cdot}62 \times 10^{6}$ N/m^2 and 163° to 5.61×10^{6} N/m^2 and 163°. Hence, the stiffness is hardly changed. The mode coefficients with $M = 128$ and 512 in Figure 15 coincide up to $n \approx 200$, where D_n is such that $D_{2n-1} = D_n^+$ and $D_{2n} = D_n^-$ (using the notations of section 2 in reference [1]). The ensuing $M = 128$ tail increase, though small, results from its truncated higher order mode compensation.

Next, the subregion method is considered with the M-extension above. Clearly, the subregion standard deviation in Figure 16 decreases faster, while the stiffness in Figure 17

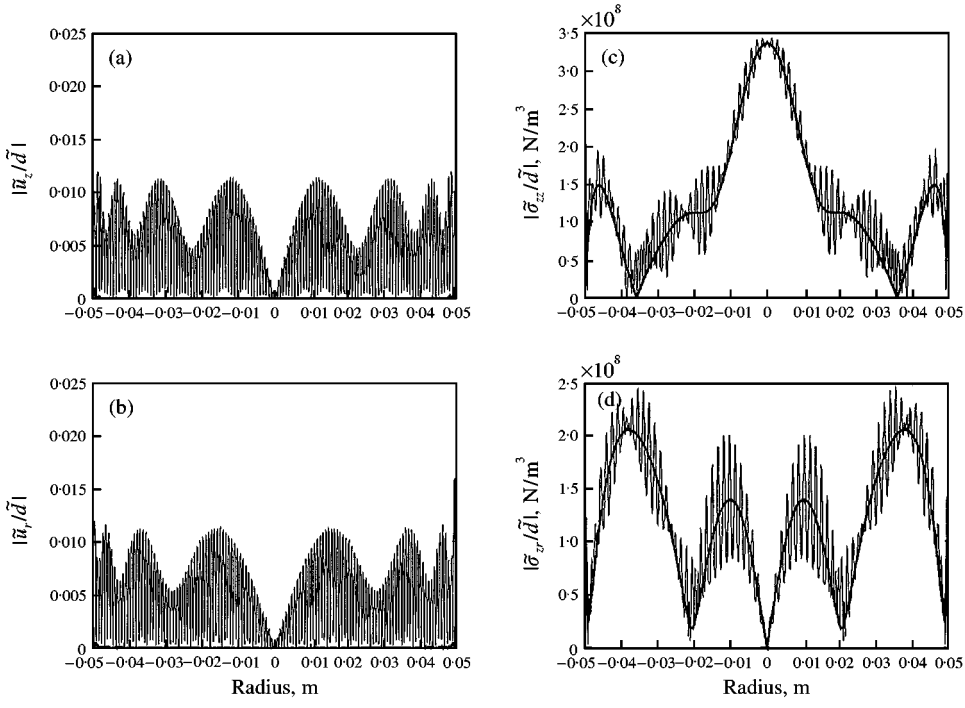

Figure 14. Magnitude of mechanical fields at $z = l/2$. Exactly determined & $M = 128$ (thin) and threefold overdetermined & $M = 512$ (thick); 1000 Hz. Normalized (a) axial displacement, (b) radial displacement, (c) axial stress and (d) radial shear stress.

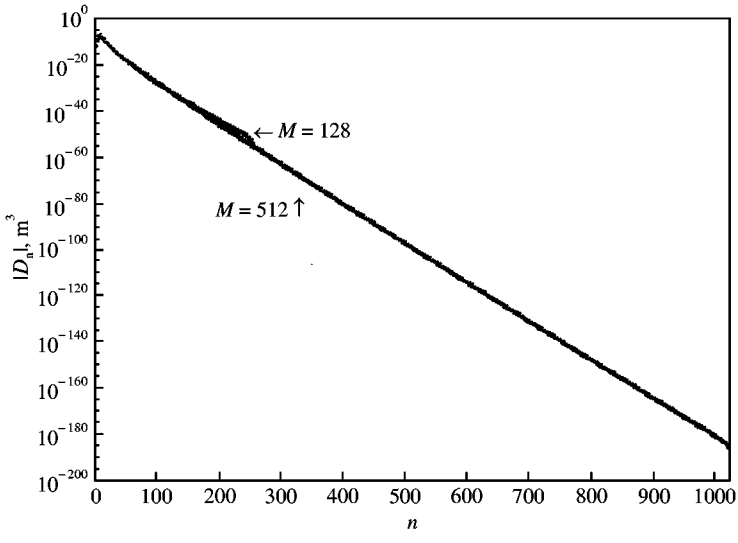

Figure 15. Magnitude of mode coefficient. Exactly determined and $M = 128$ and three-fold overdetermined and $M = 512$; 1000 Hz.

shows a higher convergence rate than for the point matching. This discrepancy diminishes, however, at over-determination, which is not surprising as its effects are similar to those of the subregion spatial integration.

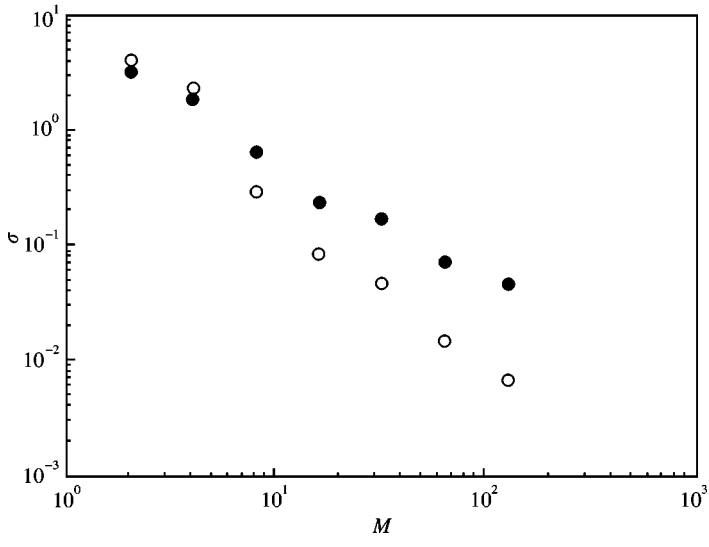

Figure 16. Normalized standard deviation of displacement residual versus total number of modes. Point matching (filled circles) and subregion method (circles); 1000 Hz.

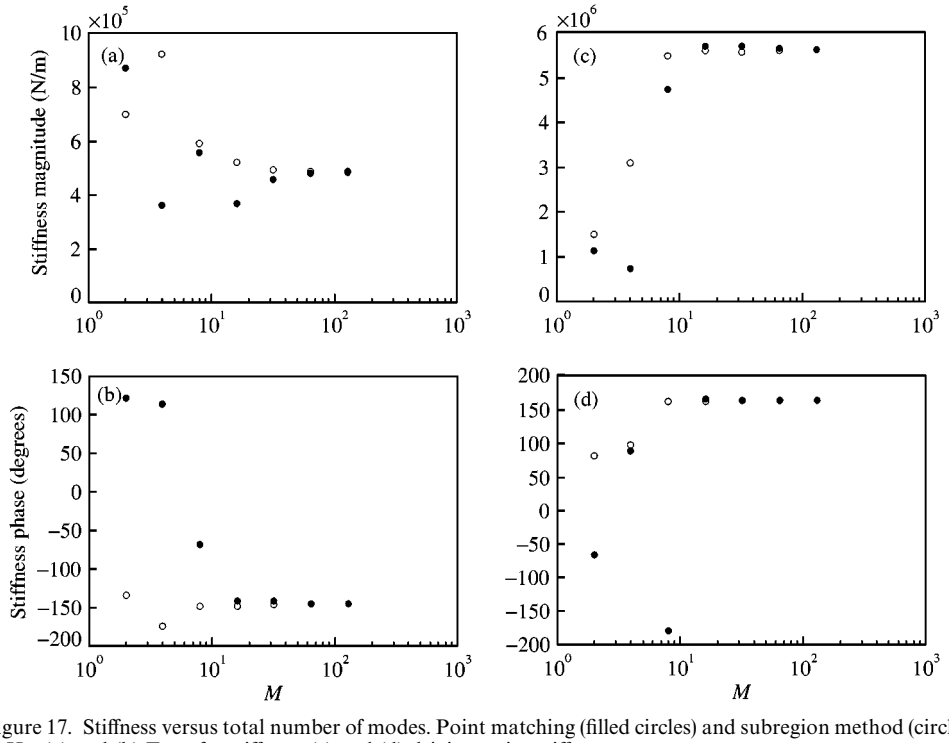

Figure 17. Stiffness versus total number of modes. Point matching (filled circles) and subregion method (circles); 1000 Hz. (a) and (b) Transfer stiffness; (c) and (d) driving point stiffness.

5. DISPLACEMENT AND STRESS FIELDS

The model governed fields, throughout the rubber cylinder ($r = 0$ to a and $z = -l/2$ to $z = +l/2$) for a wide frequency range are alternative assessments of the present model's relation to the simpler models discussed in section 3. The normalised magnitude of axial and radial displacement, calculated by point matching, using equidistant collocation radii, $P_r^1 = P_z^1 = P_r^2 = P_z^2 = 512$ and $M = 256$, are shown in Figures 18 and 19, respectively, in the frequency range of 50–10 000 Hz together with auto scaled grey bars for enhanced perceptional clarity, whereas axial and radial shear stress at 1000 Hz are in Figure 20. Clearly, the traction and displacement boundary conditions are satisfied, the radial displacement and radial shear stress vanishing at zero radius while the singular behaviour of axial stress rapidly diminishes outside ($r = a$, $z = -l/2$) and ($r = a$, $z = +l/2$) though it is noticeable only at ($r = a$, $z = -l/2$) in Figure 20, while being displayed at ($r = a$, $z = +l/2$) in Figure 14(c). The non-uniform displacement pattern in the cylinder cross-section at 50 Hz, arises mainly from the first propagating mode contortion with a pervading emphasis at 250 Hz, showing a disordered axial displacement close to the free rubber surface which eventually develops a Rayleigh surface wave at higher frequencies. Thus, the diminishing classical rod theory accuracy is already evident at 50 Hz.

Higher order propagating modes influence the total field above 250 Hz; the stiffness is, in addition, intensely influenced by higher order non-propagating modes, as discussed in section 4.

In the context of classical theory, the axial wave length at the first driving point resonance equals four cylinder lengths while equalling two at the first transfer anti-resonance. The latter has a uniform anti-node in the central cylinder cross-section. but is non-uniformly disordered in Figure 18 (500 Hz) and jointly displays a moderate radial displacement pattern, which in turn magnifies the transfer stiffness to a lesser extent than the corresponding long rod theory at ~ 500 Hz in Figure 8(a). In principle, the two ensuing transfer anti-resonances, though not present in the simplest models, are similarly explained, displaying non-uniform anti-nodes near the central cross-section, as in Figure 18 (600 Hz) for the second anti resonance.

The axial displacement shows a slightly disturbed "lumped" behaviour at 5000 Hz in Figure 18, while displaying a slightly disturbed wave characteristic at 10 000 Hz. The radial displacement fields in Figure 19 (5000 and 10 000 Hz) are influenced by the propagating modes, showing a strong axial dependence.

The mainly cylinder length independent anti-resonance at 8600 Hz is of particular interest and complexity, governing prodigious displacements in Figures 18 and 19, thereby increasing the total mode number for accurate displacement boundary condition fulfilment. In particular, M surpassed 200 (in section 3 in reference [1]) to limit the stiffness error (from an engineering point of view) to an acceptable level.

6. CONCLUSIONS

The dispersion relation solution, convergence analysis and comparison with simple models are extensively presented. Thus providing comprehensive information about the waveguide model for the dynamic isolator stiffness developed in a companion paper [1].

The dispersion relation eigenvalues are successfully calculated by a modified Newton–Raphson method to any desired accuracy with initial values given by an asymptotic expansion or a winding integral method. The winding integral search domain is split into branch-cut absent subdomains containing adaptively defined square root

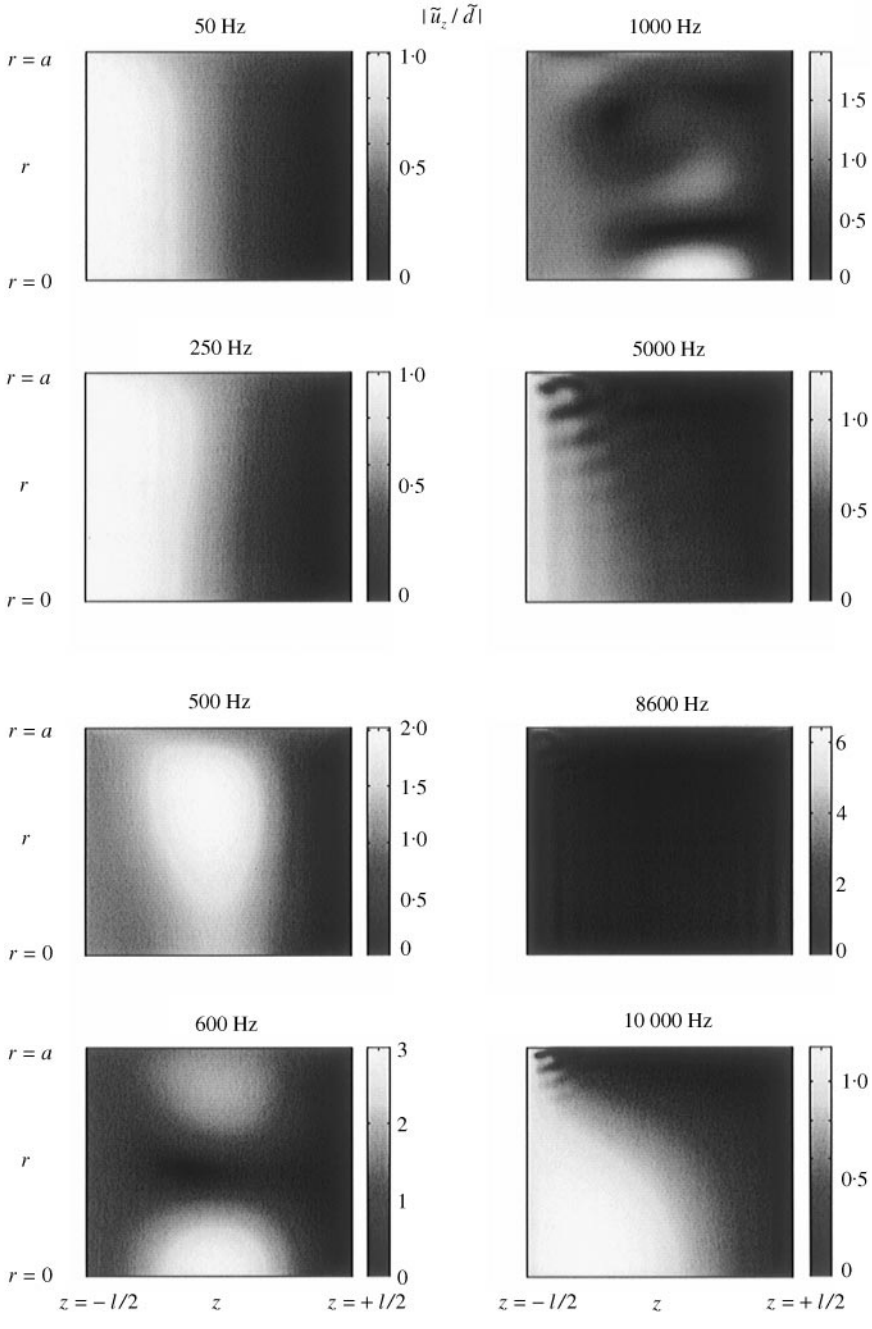

Figure 18. Magnitude of normalized axial displacement; 50–10 000 Hz.

operators. The somewhat complicated eigenvalue spectrum result displays a rapidly growing axial propagating mode number, while the first radial mode cut-on frequency is high, mainly due to the rubber material, and can be modelled as nearly incompressible with deviatoric viscoelasticity.

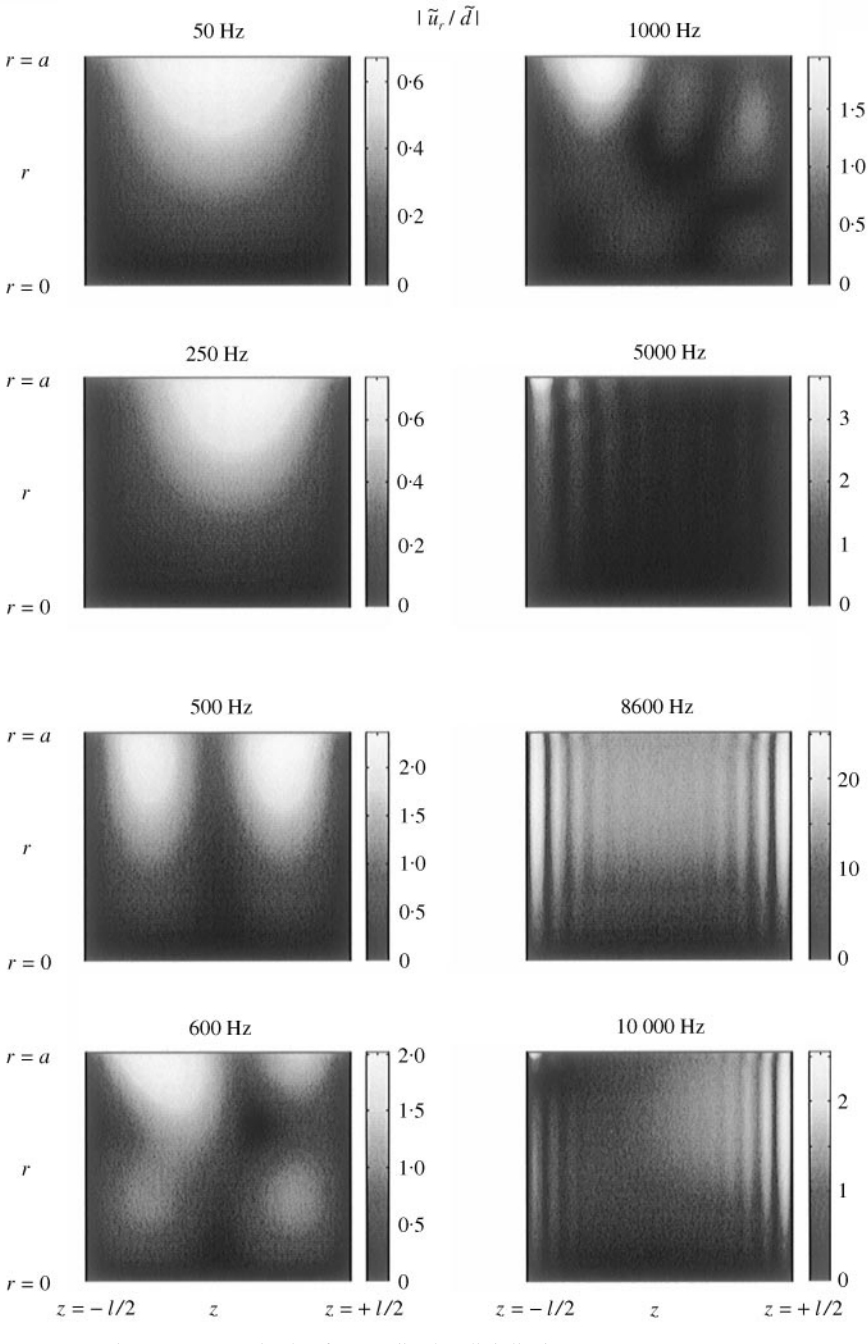

Figure 19. Magnitude of normalized radial displacement; 50–10 000 Hz.

The displacement boundary conditions at the rubber cylinder ends are satisfied by a circle-wise fulfilment or a subregion method. The latter reveals a higher convergence rate, but shows a similar rate as the former at overdetermination. In general, a moderate total mode number, such as $M = 64$, results in an accurate stiffness while point values of displacement and stress need more modes in addition to properly adapted radii, where

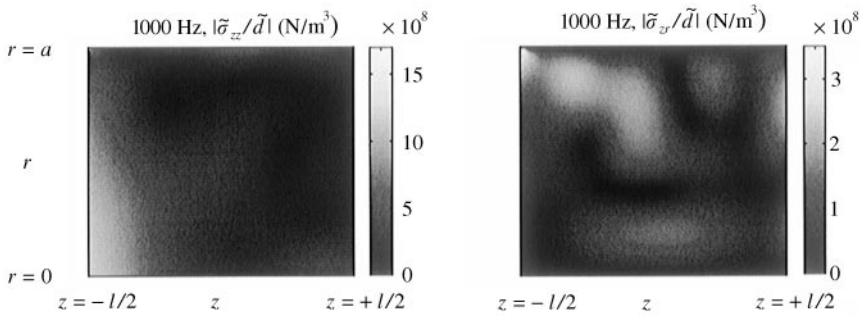

Figure 20. Magnitude of normalized stress; 1000 Hz.

overdetermined equidistant collocation is shown to be sufficient. These fields display essential spatial dependence with strong near-fields on lateral end surfaces, which are not accounted for in approximate theories, explaining the discrepancies reported in these models.

REFERENCES

1. L. KARI 2001 *Journal of Sound and Vibration* **244**, 211–233. On the waveguide modelling of dynamic stiffness of cylindrical vibration isolates. Part I. The models solutions and experimental comparison.
2. J. MIKLOWITZ 1984 *The Theory of Elastic Waves and Waveguides*. Amsterdam: North-Holland. ISBN 0-444-87513-1.
3. R. MITTRA and S. W. LEE 1971 *Analytical Techniques in the Theory of Guided Waves*. New York: MacMillan Company. LCC Card Number 70-116784.
4. L. POCHHAMMER 1876 *Journal für die reine und angewandte Mathematik* **81**, 324–336. Über die Fortpflanzungsgeschwindigkeiten kleiner Schwingungen in einem unbegrenzten isotropen Kreiszylinder.
5. C. CHREE 1889 *Transactions of the Cambridge Philosophical Society* **14**, 250–369. The equations of an isotropic elastic solid in polar and cylindrical coordinates, their solutions and applications.
6. M. ONOE, H. D. MCNIVEN and R. D. MINDLIN 1962 *Journal of Applied Mechanics* **29**, 729–734. Dispersion of axially symmetric waves in elastic rods.
7. G. DAHLQUIST and Å. BJÖRCK 1974 *Numerical Methods*. Englewood Chliffs, NJ: Prentice Hall. ISBN 0-13-627315-7.
8. S. IVANSSON and I. KARASALO 1993 *Journal of Sound and Vibration* **161**, 173–180. Computation of modal wavenumbers using an adaptive winding-number integral method with error control.
9. A. E. H. LOVE 1927 *A Treatise on the Mathematical Theory of Elasticity*. Cambridge: Cambridge University Press; Fourth Edition.
10. J. ADEM 1954 *Quarterly of Applied Mathematics* **12**, 261–275. On the axially-symmetric steady wave propagation in elastic circular rods.
11. J. C. SNOWDON 1968 *Vibration and Shock in Damped Mechanical Systems*. New York: John Wiley & Sons. LCC Card Number 68-18630.
12. R. E. D. BISHOP 1952 *Aeronautical Quarterly* **3**, 280–293. Longitudinal waves in beams.
13. G. J. KYNCH 1957 *British Journal of Applied Physics* **8**, 64–73. The fundamental modes of vibration of uniform beams for medium wavelengths.
14. R. D. MINDLIN and G. HERRMANN 1951 (cop. 1952) *Proceedings of the First U.S. National Congress of Applied Mechanics*, 187–191. A one-dimensional theory of compressional waves in an elastic rod.
15. R. D. MINDLIN and H. D. MCNIVEN 1960 *Journal of Applied Mechanics* **27**, 145–151. Axially symmetric waves in elastic rods.
16. K. F. GRAFF 1991 *Wave Motion in Elastic Solids*. New York: Dover Publications. ISBN 0-486-66745-6. Reprint.

17. J. ZEMANEK Jr 1972 *Journal of the Acoustical Society of America* **51**, 265–283. An experimental and theoretical investigation of elastic wave propagation in a cylinder.
18. E. VOLTERRA 1955 *Ingenieur-Archiv* **23**, 410–420. A one-dimensional theory of wave-propagation in elastic rods based on the method of internal constraints.
19. B. SZABÓ and I. BABUŠKA 1991 *Finite element Analysis*. New York: John Wiley & Sons. ISBN 0-471-50273-1.